ASTRONOMY & ASTROPHYSICS
SUPPLEMENT SERIES

Astron. Astrophys. Suppl. Ser. **136**, 269–284 (1999)

A survey of the ISM in early-type galaxies

II. The dust

F. Ferrari[1], **M.G. Pastoriza**[1], **F. Macchetto**[2,3], **and N. Caon**[4]

[1] Instituto de Física, UFRGS, Porto Alegre, Brazil
[2] Space Telescope Science Institute
[3] On assignment from the Space Science Department of ESA
[4] Instituto de Astrofísica de Canarias, Tenerife, Spain

Received May 11, 1998; accepted January 4, 1999

Abstract. We present results of a CCD optical imaging survey of the dust content in 22 early-type luminous galaxies, selected from the RC3 Catalog. A large fraction (75%) of the observed galaxies show significant amounts of dust. The morphology and size of the dust distribution of the observed galaxies follows very closely that of the ionized gas. For each galaxy, we have used broad band V and R filters imaging to build colour maps and determine the A_V and A_R extinction maps. We have found typical A_V values of 0.026 and A_R of 0.023 and have derived $(V-R)$ values in the range $0.49-0.68$. The A_V values together with an assumption of the dust grain size and composition enable us to estimate the dust masses. We have studied the correlations between the mass of dust and the Hα, IR and $L_{\rm B}$ luminosities. Finally, we investigate the possible mechanisms responsible for the dust emission.

Key words: galaxies: elliptical and lenticular — galaxies: ISM — dust extinction — surveys

1. Introduction

Several authors have investigated the presence of the interstellar medium (ISM) in early-type galaxies. In particular, Goudfrooij et al. (1994b) have detected dust lanes and patches in 23 galaxies (41% of their sample) using colour index images, within a detection limit $A_{\rm B}=0.02$. The analysis of the wavelength dependence on the extinction shows that the extinction curves run parallel to the Galactic curve. R_V was found to be 2.5 in average, which is lower than the canonical Galactic value of 3.1, implying that the large grains, responsible for the extinction in the visible, are smaller than those in our galaxy (Goudfrooij et al. 1994c). They found typical dust masses in the range $10^3-10^5 M_\odot$. Recently these results were confirmed by HST data, which showed that 78% of the early-type galaxies contain nuclear dust (Van Dokkum & Franx 1995).

Dust masses derived from the IRAS flux densities are found to be roughly an order of magnitude higher than those derived from the optical extinction values. This is in strong contrast from the situation in spiral galaxies. To account for this difference it was argued that most of the dust in elliptical galaxies exists as a diffuse component undetectable at optical wavelengths. This diffuse dust component produces a radial colour gradient that adds to the gradient produced by metallicity and age variations, as shown by Goudfrooij et al. (1995).

Several elliptical galaxies which show evidence for dust have isophotal properties and kinematics consistent with the current accepted merger model for these galaxies (Forbes 1991). Furthermore, it has been shown that the apparent rotation axis of the dust (as derived from the orientation of the dust lane) does not generally coincide with that of the stars. This suggests an external origin for the dust (Van Dokkun & Franx 1995).

We have previously studied the ionized gas for a large sample of 73 early-type galaxies (Macchetto et al. 1996, hereafter referred to as Paper I) and found it to be present in most elliptical (72%) and lenticular (85%) galaxies. The gas distribution appears to range from small disks (SD) to regular extended (RE) and filamentary (F) structures. The gas mass ranged from 10^3 to 10^5 $M_\odot$. Correlations between the warm and hot gas components and the total Hα and X luminosities were investigated: we found that galaxies rich in Hα are also X-ray emitters, while there are X-ray bright objects lacking ionized gas.

In this paper, we present results of CCD observations of 15 elliptical and 7 lenticular galaxies from the sample in Paper I, for which we have obtained deep images in both V and R bands,which are necessary for this study. We will carry out observations of the other galaxies in Paper I in the future. We have explored the correlations between the masses of the dust and ionized gas and the IR and blue luminosities.

This paper is structured as follows: in Sect. 2 we present the galaxy sample, in Sect. 3 we discuss the observations and data reduction. The description of individual galaxies is given in Sect. 3.3. The dust mass determination is presented in Sect. 4. The correlations between the dust masses and the $L_{\rm B}$, $L_{{\rm H}\alpha}$ $L_{\rm IR}$ luminosities are presented in Sect. 5. In Sect. 6 we discuss the dust heating mechanism, while concluding remarks are given in Sect. 7.

2. The sample

The early-type galaxies studied in this article are a subsample of the galaxies studied in Paper I, for which we have very reliable V and R images. They are luminous galaxies ($B_{\rm T} < 13$ mag) with morphological type E and S0 taken from "The Third Reference Catalog of Bright Galaxies" (RC3; de Vaucouleurs et al. 1991) and the "Revised Shapley-Ames Catalog" (RSA; Sandage & Tammann 1987). The galaxies, their morphological types, magnitudes, coordinates and distances are listed in Table 1. The distances have been derived with the "220 model" for the Virgo Infall of Kraan-Korteweg (1986) assuming that Virgo Cluster is at a distance of 21.3 Mpc, which implies a Hubble constant $H_0 = 55\,{\rm km\,s^{-1}\,Mpc^{-1}}$. For galaxies not present in the Kraan-Korteweg's list, distances were derived from their redshift corrected to the reference frame defined by the cosmic microwave radiation (from RC3).

3. Observations, colour-index $(V-R)$, A_V and A_R extinction maps

3.1. Observations

The images of our galaxies were acquired using broad–band V and R filters matching the Cousins standard bands during the same runs described in Paper I. The observational set-ups and filters specifications are given in Tables 1, 2 and 4 of Paper I. The exposure times for each galaxy were chosen to be 30 and 300 s, with 30 s optimized to obtain the images in the very central part of each galaxy and 300 s optimized for the external regions, since in these longer exposures the center was saturated. The data was processed with IRAF[1], using the standard techniques for bias and dark-current subtraction, division by normalized twilight flat-fields, and interpolation over bad columns and pixels. No pattern was found in the bias frames.

Table 1. Identification, coordinates, morphological type and distance from RSA catalog and the blue apparent magnitude $B^0_{\rm T}$, corrected for Galactic absorption and redshift, for the galaxies in the sample

Ident	RA(2000)	DEC(2000)	type	D (Mpc)	$B^0_{\rm T}$
NGC 533	01 25 31.5	+01 45 35	E3	44.1	12.22
NGC 636	01 39 06.6	−07 30 47	E1	33.2	12.22
NGC 1600	04 31 39.9	−05 05 16	E4	83.9	11.83
NGC 2865	09 23 30.8	−23 09 48	E4	48.4	12.18
NGC 3268	10 30 00.6	−35 19 30	E2	57.5	12.26
NGC 3311	10 36 43.3	−27 31 41	S0	63.9	12.22
NGC 3379	10 47 49.9	+12 34 57	E0	14.5	10.18
NGC 3489	11 00 18.2	+13 54 08	S0/Sa	9.2	11.15
NGC 3607	11 16 54.1	+18 03 12	S0	14.7	10.79
NGC 4472	12 29 46.5	+07 59 58	E1/S0	21.3	9.33
NGC 4473	12 29 48.8	+13 25 49	E5	21.3	11.03
NGC 4552	12 35 39.9	+12 33 25	S0	21.3	10.57
NGC 5044	13 15 24.0	−16 23 09	E0	52.2	11.67
NGC 5812	15 00 55.8	−07 27 29	E0	40.7	11.83
NGC 5813	15 01 11.2	+01 42 08	E1	34.9	11.42
NGC 5903	15 18 36.3	−24 04 06	E3/S0	44.3	11.74
NGC 6483	17 59 29.8	−63 40 07	E	85.2	12.63
NGC 6758	19 13 52.3	−56 18 33	E2	58.8	12.31
NGC 6909	20 27 38.7	−47 01 34	E5	48.6	12.51
IC 4797	18 56 29.3	−54 18 22	E pec	46.6	11.85
IC 4889	19 45 15.9	−54 20 37	S0	43.5	11.91
IC 5105	21 24 22.2	−40 32 11	E5	93.5	12.42

3.2. Colour maps $(V-R)$

To build the $(V-R)$ colour maps, we first realigned the V and R images, by measuring the centers of field stars with similar point spread function (PSF) in each image. The centering was accurate up to a tenth of a pixel for most galaxies, except for NGC 2865 and NGC 4472 whose frames contain too few field stars to perform the alignment. In this case the central part of the galaxy and other obvious morphological visible features were used to define the alignment. For images with different seeing the PSFs were matched before the subsequent analysis. The background counts were estimated by measuring boxes in regions of the images not affected by the galaxy luminosity. This is a reliable procedure since most of our images have no gradient in the backgrounds, except for NGC 3311 and NGC 4472, where a power law of degree 1 was fitted to the outer galaxy profiles in order to estimate and subtract the background. The images were calibrated using multi-colour and multi-aperture photometry of Poulain (1986, 1988) and Poulain & Nieto (1994) as described in Paper I. Once the background was subtracted we created the $(V-R)$ colour-index map, used to determine the morphology and size of the dust distribution when

---

[1] IRAF is distributed by the National Optical Astronomy Observatories, which is operated by the Association of Research in Astronomy, Inc., under cooperative agreement with the National Science Foundation, U.S.A.

calculating the dust masses. The contribution of the ionized gas emission to the colour maps can be neglected, since the R filter width is roughly 1500 Å and the equivalent width of the emission lines, summed together, is not more than 15 Å, thus, this contamination is less than 1% or 0.01 mag. Figure 5 shows the V and $(V-R)$ isophotes as well as the Hα + [NII] emission maps from Paper I for each galaxy, except for NGC 2865, NGC 6483, NGC 6909 and IC 4797, which do not show Hα + [NII] emission. North is up and East to the left for all images. The V and $V-R$ contour levels are listed while for Hα + [NII] we show the lowest contour level, which corresponds to the flux threshold level, in units of $10^{-16}\,\mathrm{erg\,s^{-1}arcsec^{-2}}$. The central blank regions in the colour maps of some galaxies are due to an overexposure of the nucleus.

3.3. Dust morphology and description of individual cases

The redder $(V-R)$ values in the colour index maps (Fig. 5) correspond to larger A_V and A_R extinction values. From these maps we observe that the dust is in the form of filaments (e.g. NGC 533, NGC 4472 and NGC 5044), small disks (e.g. NGC 3379) and regular extended clouds (e.g. NGC 636, NGC 3311). The dust morphology follows very closely that of the ionized gas. We have measured the typical size l of the dust distribution (Table 2) which corresponds to the size of the most external isophote as shown in the $(V-R)$ maps, and found that the dust has roughly the same size and distribution as that of the ionized gas.

Since the dust morphology varies considerably amongst the galaxies of our sample, it is worth to describe the most interesting cases separately. We use the same classification of Paper I, according to morphology and size:

- small disk (SD): faint and short filaments, mean diameter $\leq$ 4 Kpc;
- regular extended (RE): similar to SD but larger in size (4 to 8 Kpc);
- filaments (F): conspicuous filamentary structure, often extending as far as 10 Kpc from the galaxy center.

NGC 533. This galaxy has a filamentary dust distribution. Its morphology and distribution corresponds to that of the ionized gas.

NGC 636. The dust distribution is asymmetric with a cone-like shape oriented in the SE direction, while the ionized gas is in the form of a small disk, whose major axis orientation is perpendicular to the axis of the cone.

NGC 1600. The dust extends farther than 15″ with an asymmetric filamentary structure in the W direction, while the Hα emission is located in a small $5'' \times 5''$ central disk.

NGC 2865. There is a large fragmentary dust cloud extending up to 15″ from the nucleus. The asymmetric pattern of the cloud is due to the presence of a very bright field star in the SW direction. No ionized gas is observed in this galaxy.

NGC 3268. A small disk of dust and ionized gas is observed in the inner 5″ of this galaxy. Note that the dust distribution is asymmetric with respect to the major axis of the galaxy in the SE direction, the opposite is observed for the ionized gas. The dust disk absorption can be seen in the inner V isophote.

NGC 3311. The dust cloud has an elongated structure oriented along the NS direction while the ionized gas cloud is roughly spherical, with a weak absorption feature which coincides with the dust pattern.

NGC 3379. The dust is concentrated in a large asymmetric cloud in the S direction. The Hα image shows a very clear absorption feature South of the nucleus of the galaxy.

NGC 3489. This is an S0/Sa type galaxy. It has a very complex absorption pattern which has the form of patches (in the E side) and extended filamentary structure (in the W side). The dust absorption is observed also in the V image of the galaxy, producing box shaped isophotes in the central 20″ of the galaxy (see the V isophotes map in Fig. 5). The ionized gas distribution in the form of filaments is rather regular in the inner 20″, in which some patches of absorption can be seen.

NGC 3607. This is another case where the dust and ionized gas have the form of an asymmetric small disk. The dust absorption is stronger in the NE direction, while the ionized gas emission is stronger in the SW direction.

NGC 4472. This galaxy dust cloud is in the form of a small disk, similar to that of the ionized gas, although smaller in size.

NGC 4473. It shows a very small and edge on dust disk which is clearly observed in the ionized gas isophotal maps.

NGC 4552. This is an S0 galaxy with a very small amount of absorption at our limit of detection, in the form of filaments, more elongated to the NE direction, while the gas extends farther to the SW.

NGC 5044. The dust distribution has an irregular morphology, concentrated in the inner 10″. Two central dark clouds can be seen. This galaxy has a very bright ionized gas emission in the form of extended filaments up to 40″ from the center, being larger in the southern part of the galaxy. This galaxy seems to have gas and dust mixed, although the morphology of the ionized gas is not produced by dust absorption, since the dust cloud is smaller than the ionized gas emission region.

NGC 5812. The dust is distributed regularly in an inner region of 13″ and is more extended than the ionized gas cloud. However, both have the same overall morphology.

NGC 5813. This is another case of an asymmetric distribution of the dust absorption in the form of filaments. The denser dust clouds follow the ionized gas distribution.

NGC 5903. The dust lies in a region smaller than that spanned by the ionized gas cloud, showing a similar morphology.

NGC 6483. This galaxy shows a irregular and filamentary dust distribution, more elongated in the SW direction. No gas is observed in this galaxy.

NGC 6758. An asymmetric dust disk can be seen in this galaxy, extending to the SW direction, while the gas is distributed in a more homogeneous cloud.

NGC 6909. The dust is in a small disk oriented with its edge on, elongated in the E direction. No gas is observed for this galaxy.

IC 4797. This galaxy has a filamentary dust distribution which seems to be obscured in the NE direction, although no gas is observed in this case.

IC 4889. This S0 galaxy shows a very large absorption cloud extending to the NE side of the galaxy. It also has a very bright and extended ionized gas emission. The unextinguished area in the southern part of the galaxy coincides with the brightest emission region of the galaxy.

IC 5105. This galaxy shows a very strong morphological correlation between the dust and the ionized gas clouds. Two large absorption regions extend to the NW and SE sides of the galaxy, separated by a narrow emission region. The inverse pattern is generally observed in the central parts of the other galaxies in our sample.

4. Determination of A_V and of the dust mass

The determination of the extinction in both passbands requires comparing the unaffected light with the extinguished one. Assuming that the isophotes of the observed galaxies are intrinsically ellipses, it is possible to build a model image adjusting ellipses to the isophotes of the galaxy. This fitting is done with the *isophote* routines in the STSDAS package within IRAF. This model image represents the light not extinguished by the dust, since it is not affected by local intensity irregularities caused by the dust absorption and scattering. With this model image it is possible to construct extinction maps in both filters for each galaxy

$$A_\lambda = -2.5 \log \left[\frac{F_{\lambda,\mathrm{obs}}}{F_{\lambda,\mathrm{model}}} \right] \tag{1}$$

where F is the count level for each image pixel. The flux calibration and sky background are not relevant for the extinction maps, since the model incorporates them. In the galaxies with isophotes strongly affected by the dust (e.g. NGC 3489, NGC 5044), the first model was used to identify the dust distribution to be masked in further fittings, at least in the regions where the *isophote* routines do not easily converge.

The mean A_V and A_R values derived from the dust maps are listed in Table 2 as well as the mean $(V-R)$ values. Note that the standard deviations are not due to errors, but due to the fact that the extinction is not uniform over the region used in the measurements. The particle density N_d of the dust cloud can be estimated by making simple assumptions about the physical properties of the dust grains together with the mean A_V value inside the dust region, as follows.

The theoretical model to compute A_V assumes that it is proportional to the optical cross section C_ext weighted by the grain size distribution $n(a)$, integrated over the grain sizes ($a_- < a < a_+$) along the dust cloud length l in the line of sight. Assuming $n(a)$ to be the same for the whole cloud and using the definition of the efficiency factor $Q_\mathrm{ext}(a,\lambda) = C_\mathrm{ext}(a,\lambda)/\pi a^2$, i.e., the ratio between the extinction and the geometrical cross sections, A_λ can be written (Spitzer 1978) as:

$$A_\lambda = 1.086\, l \int_{a_-}^{a_+} Q_\mathrm{ext}(a,\lambda)\, \pi a^2\, n(a)\, \mathrm{d}a. \tag{2}$$

The efficiency factor is related to the grain sizes and composition and varies with wavelength. Q_ext must be parameterized according to the sizes and optical properties of the grains. In the optical region, assuming that the extinction is caused mainly by silicates (Mathis et al. 1977), Q_ext can be assumed to vary as (Goudfrooij et al. 1994c):

$$\begin{aligned} Q_{V,\mathrm{ext}} &= \begin{cases} 0.8\, a/a_{Si} & a < a_{Si} \\ 0.8 & a > a_{Si} \end{cases} \\ a_+ &= 0.22\,\mu\mathrm{m} \\ a_- &= 0.005\,\mu\mathrm{m} \\ a_{Si} &= 0.1\,\mu\mathrm{m}. \end{aligned} \tag{3}$$

Since the extinction curves of elliptical galaxies in the optical region are similar to that of our Galaxy (Goudfrooij et al. 1994), we can also use the same grain size distribution. Mathis et al. (1977) demonstrated that the function which best reproduces the extinction curve of our Galaxy over a wide range of wavelengths is

$$n(a) = n_0\, a^{-3.5} \tag{4}$$

where

$$N_\mathrm{d} = \int_{a_-}^{a_+} n(a)\, \mathrm{d}a. \tag{5}$$

By means of Eq. (2) and Eq. (4) N_d can then be evaluated. Eq. (5) is used to compute the normalization factor n_0 introducing N_d into Eq. (2). We measured the extinction A_V as the mean value of the absorption features in the extinction maps and estimated the associated dust cloud size l from the colour map $(V-R)$. Using these parameters and those previously derived in this section, we evaluate the mass density ρ and the total mass M_dust of the dust cloud.

The derived dust mass ranges between 10^3 and $10^5\ M_\odot$. These values are comparable to the ionized gas mass derived in Paper I. The good correlation between M_dust and M_HII (Fig. 2) suggests that both ISM components are intrinsically related.

Table 2. Measured values of the extinction A_V and A_R, the colour index $(V-R)$, the mean size l of the dust cloud, the dust mass and the cloud morphology for the galaxies of the sample. Morphology: SD – Small discs, F – Filamentary, RE – Regular extended; Scale relative to gas distribution (Paper I): $\star$ – larger, † – equal, ‡ – smaller. (Values inside parentheses are at our limit of detection)

Galaxy	$\bar{A_V} \pm \sigma_{A_V}$	$\bar{A_R} \pm \sigma_{A_R}$	$(V-R) \pm \sigma_{(V-R)}$	$\bar{l}$ (Kpc)	$\log M(M_\odot)$	Morphology
NGC 533	0.022 ± 0.023	0.012 ± 0.010	0.563 ± 0.04	$9.6^\star$	4.84	F
NGC 636	0.021 ± 0.019	0.036 ± 0.036	0.679 ± 0.09	$3.4^\star$	3.91	RE
NGC 1600	0.034 ± 0.030	0.021 ± 0.018	0.634 ± 0.01	$18.6^\star$	5.61	F
NGC 2865	0.016 ± 0.016	0.013 ± 0.011	0.622 ± 0.01	6.0	4.30	RE
NGC 3268	0.009 ± 0.008	0.006 ± 0.005	0.666 ± 0.03	$2.2^\dagger$	3.17	SD
NGC 3311	0.014 ± 0.012	0.018 ± 0.019	0.661 ± 0.02	$2.5^\dagger$	3.50	RE
NGC 3379	0.027 ± 0.035	0.028 ± 0.032	0.597 ± 0.03	$(1.1)^\ddagger$	(1.97)	SD
NGC 3489	0.084 ± 0.052	0.097 ± 0.063	0.522 ± 0.05	$1.2^\star$	3.91	F
NGC 3607	0.015 ± 0.012	0.017 ± 0.020	0.615 ± 0.03	$(1.7)^\dagger$	(3.20)	SD
NGC 4472	0.009 ± 0.008	0.010 ± 0.009	0.610 ± 0.01	$(1.9)^\ddagger$	(3.03)	SD
NGC 4473	0.017 ± 0.014	0.016 ± 0.015	0.668 ± 0.03	$(1.5)^\dagger$	(3.15)	SD
NGC 4552	0.017 ± 0.015	0.018 ± 0.016	0.607 ± 0.03	$(1.3)^\ddagger$	(3.01)	F
NGC 5044	0.013 ± 0.011	0.008 ± 0.007	0.661 ± 0.02	$5.2^\ddagger$	4.08	F
NGC 5812	0.016 ± 0.019	0.008 ± 0.009	0.658 ± 0.05	$5.1^\star$	4.15	RE
NGC 5813	0.020 ± 0.018	0.014 ± 0.014	0.658 ± 0.05	$4.3^\ddagger$	4.11	RE
NGC 5903	0.040 ± 0.044	0.039 ± 0.044	0.648 ± 0.06	$3.3^\ddagger$	4.17	RE
NGC 6483	0.030 ± 0.026	0.025 ± 0.023	0.615 ± 0.05	8.7	4.89	F
NGC 6758	0.006 ± 0.005	0.014 ± 0.010	0.664 ± 0.09	$4.3^\star$	3.58	RE
NGC 6909	0.042 ± 0.033	0.028 ± 0.020	0.495 ± 0.03	1.7	3.61	SD
IC 4797	0.049 ± 0.051	0.029 ± 0.029	0.603 ± 0.07	3.4	4.29	F
IC 4889	0.021 ± 0.017	0.016 ± 0.011	0.686 ± 0.03	$6.9^\ddagger$	4.54	RE
IC 5105	0.022 ± 0.021	0.010 ± 0.009	0.615 ± 0.04	$12.9^\star$	5.10	RE

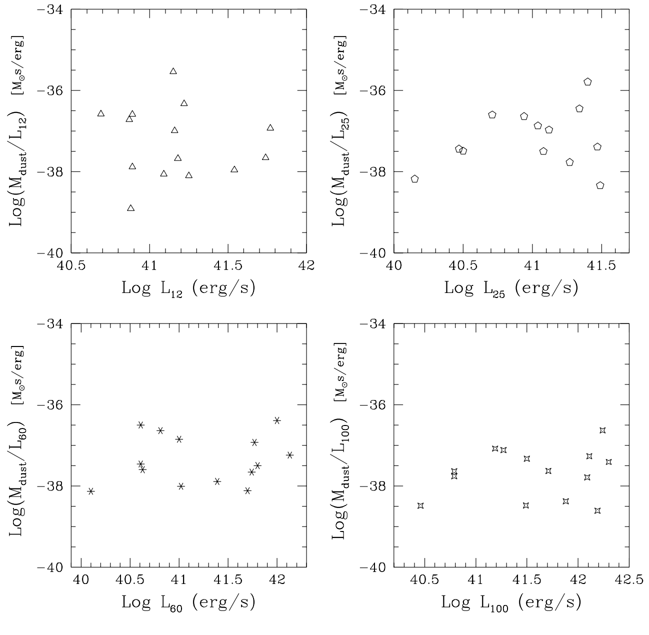

Fig. 1. The ratio between the mass of the dust and the IRAS luminosity as a function of and the IRAS luminosity at different wavelengths

5. L_{IR}, $L_{H\alpha}$ and $M_{\rm dust}$ relation

Our sample covers a large range of galaxy distances $9.2 < D < 93$ Mpc (Table 1). This fact can introduce spurious correlations if luminosity-luminosity or mass-luminosity relations are used, since both mass and luminosity scale with the distance squared. To avoid this, the plots are mass-luminosity ratio vs. luminosity. In this way, as the only distance dependent axis is that of the luminosity, a constant behavior would indicate that the mass really increases with luminosity. For this sample we have investigated the relationship between the IRAS luminosities and the dust mass in Fig. 1. There is a general trend of increasing mass with increasing IR luminosity. However the scatter is large. Note that the correlation becomes tighter with increasing wavelength. At 12 μm there may not even be a correlation, the two observed branches could be attributed to a contributions from the stellar population of the galaxies. At longer wavelengths the stellar component decreases and the dust emission dominates. Since the correlation improves towards 100 μm, the IR emission peak of the dust must be beyond 100 μm, indicating a cold dust, with temperature $T_{\rm dust} < 23$ K, assuming a black body law.

Figure 2 shows that comparable amounts of dust and ionized gas are found in the central region of these galaxies. The total mass for these two components are

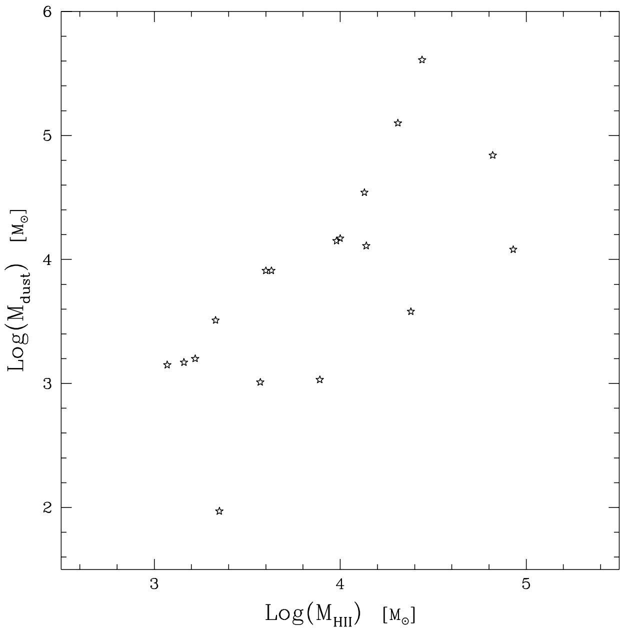

Fig. 2. Relation between the H II and the dust masses

in the range $2\,10^3 - 5\,10^5$ for the observed sample. This correlation is not produced by the distance effect mentioned earlier, as it shows up with the same strength in a flux-flux diagram.

The causal relationship between the dust content and the current stellar population of the galaxy sample can be inferred from the absence (Goudfrooij & de Jong 1995; Forbes 1991) or presence of a correlation between the dust mass and the blue luminosity of elliptical galaxies. We investigated this relationship (Fig. 3) and plotted the logarithm of the ratio of the dust mass to the blue luminosity as a function of the total blue luminosity and also as a function of the blue luminosity computed inside the emitting region (Table 5 of Paper I). Both plots suggest a correlation between the dust mass and the galaxy blue stellar population, which disagrees with the results of Goudfrooij & de Jong (1995).

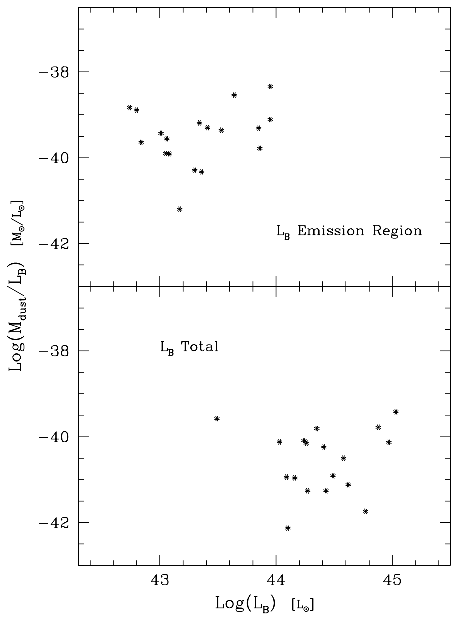

Fig. 3. The mass of the dust normalized by the corresponding blue luminosity is plotted as a function of the blue luminosity measured inside the emitting region (upper panel) and the total blue luminosity of the galaxy (lower panel)

Table 3. The UV luminosity, the calculated and observed infrared luminosities, and the effective optical depth

Ident	$\log L_{\rm UV}$	$\log L_{\rm IR}^{\rm calc}$	$\log L_{\rm IR}^{\rm W}$	$\log L_{\rm IR}^{\rm C}$	$\tau_{\rm eff}$
NGC 533	52.31	42.20	42.07	42.10	0.10
NGC 1600	51.94	41.91	42.04	42.25	0.16
NGC 3311	50.82	39.26	41.62	41.83	0.06
NGC 3379	50.84	40.63	40.43	40.48	0.12
NGC 4472	51.38	40.82	40.62	40.66	0.04
NGC 4473	50.56	39.71	42.02	41.37	0.08
NGC 4552	51.06	40.43	39.89	40.22	0.08
NGC 5044	52.42	42.98	41.79	41.79	0.06
NGC 5812	51.47	40.65	41.19	41.15	0.07
NGC 5813	51.64	41.55	40.88	41.04	0.09
NGC 5903	51.49	41.59	41.19	41.36	0.18
NGC 6758	51.87	41.61	41.76	42.12	0.03

6. Dust heating mechanism

There are several mechanisms that in principle could account for the dust heating, among them the evolved hot star populations. However Binette et al. (1994) developed a starburst evolution model and showed that Post-AGB stars are by far the main source of UV photons at an age of 10^{10} years, while other sources, such as nuclei of planetary nebulae can contribute significant amounts of UV photons for ages up to $2\,10^9$ years. There are also other alternatives, such as hot electrons in hot emitting gas or exposed hot cores (10^5 K) of post red giant stars. The problem with the latter two mechanisms is that they will also produce X-ray emission, which is only observed for a small number of galaxies in this sample.

In Paper I we found a strong correlation between the Hα + [NII] luminosity and the luminosity in the B band, inside the region occupied by the line emitting gas. We also demonstrated that Post-AGB stars provide enough ionized radiation to account for the observed Hα luminosity. In most cases there were considerably more UV photons available than those needed to produce the observed $L_{\mathrm{H}\alpha}$ (typically by a factor of $1.5-2$). This excess of UV photons are available to heat the dust which then reprocesses these photons reemiting them at IR wavelengths. The correlation between the dust mass and the blue luminosity inside the emitting region, shown in Fig. 3, is exactly as expected if the post-AGB stars are the main source of the UV photons and also heat the dust.

A simple estimate for dust luminosity can be obtained by assuming a model where the dust is distributed roughly uniformly around the sources or concentrated in spherically symmetric dust clouds. The total energy absorbed by the dust and reemited in the infrared (L_{IR}) is related to the total incident UV luminosity (L_{UV}) as (Bonatto & Pastoriza 1997)

$$\frac{L_{\mathrm{IR}}}{L_{\mathrm{UV}}} = \frac{\Omega}{4\pi}\,(1 - \mathrm{e}^{-\tau_{\mathrm{eff}}}) \qquad (6)$$

where Ω is the solid angle subtended by the dust distribution and τ_{eff} is the effective optical depth to the incident UV/optical continuum along the line of sight. The optical depth is defined as $\tau_{\mathrm{eff}} = A_{\mathrm{UV}}/1.086$ and assuming a Galactic extinction law $A_{\mathrm{UV}} \simeq 5\,A_V$. The visual extinction was computed from the extinction maps (see Table 2). The UV photons emited by post–AGB stars were calculated from $L_{\mathrm{H}\alpha}^{\mathrm{calc}}$ (see Table 5 of Paper I) using recombination theory (Osterbrock 1974).

$$L_{\mathrm{UV}} = \frac{L_{\mathrm{H}\alpha}}{h\nu_{\mathrm{H}\beta}}\,\frac{1}{2.85}\,\frac{\alpha_{\mathrm{B}}(\mathrm{H^0T})}{\alpha_{\mathrm{H}\beta}(\mathrm{H^0T})} \qquad (7)$$

where $\alpha_{\mathrm{B}}(\mathrm{H^0T})$ and $\alpha_{\mathrm{H}\beta}(\mathrm{H^0T})$ are the recombination coefficients. From the $L_{\mathrm{UV}}^{\mathrm{calc}}$ emited by the post–AGB stars we have computed the $L_{\mathrm{IR}}^{\mathrm{calc}}$, using Eq. (6). From the observed IRAS fluxes we can compute the two components of the IR luminosities, namely the warm component $L_{\mathrm{IR}}^{\mathrm{W}}$, which assumes that most of the dust emission is produced at 25 and 60 μm, and the cold component $L_{\mathrm{IR}}^{\mathrm{C}}$, derived from the 60 and 100 μm luminosities, as in Bonatto & Pastoriza (1997). Figure 4 shows a good agreement between the calculated and both of the observed IR luminosities for most of the galaxies, except NGC 3311 and NGC 4473 at the lower right, which seem to have a very luminous IR emission.

This simple calculation suggests that post–AGB stars are an ideal source of ionizing photons for the gas and heating photons for the dust. The post–AGB stars are known to exist and are distributed throughout the galaxy as the old stellar population thus providing in-situ sources of ionizing photons. This does, of course, not prove that they are the only mechanism capable of producing the observed dust emission and indeed more than one mechanism is likely to contribute in different amounts in each individual galaxy.

7. Conclusions

We have shown the results of a CCD optical imaging survey of the dust content in 22 elliptical and S0 luminous galaxies. A large fraction (75%) of the observed galaxies have dust contents in the form of small disks, regular extended and filamentary structures. The morphology and size of the dust distribution of the observed galaxies follows very closely that of the ionized gas. For each galaxy, we have used broad band V and R filters imaging to build colour maps and derive the $(V-R)$ colour map, A_V and A_R extinction maps. We have found typical A_V values of 0.026, A_R of 0.023. The A_V values together with simple assumption about the dust grain size and composition enables us to estimate the dust masses. We derived values in the range $10^3 - 10^5\ M_\odot$ We have studied the correlations between the dust mass and the Hα, IR and L_{B} luminosities.

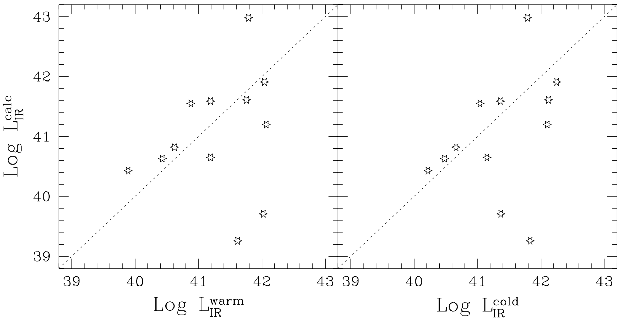

Fig. 4. Relation between the observed and calculated infrared luminosities

We found that the correlation between the IRAS luminosity and the dust mass is enhanced from 25 μm to 100 μm. Since the correlation improves towards 100 μm it suggests that the peak of the dust emission might be beyond 100 μm, thus the dust temperature is below $T = 23$ K, assuming a black body law.

We also found that post–AGB stars provide sufficient UV radiation to heat the dust, as well as to ionize the gas, to account for the observed IR luminosity, which in turn explains the correlations between the dust mass, the blue luminosity and the infrared luminosity for the galaxy sample.

Acknowledgements. These observations were obtained at the ESO telescopes in La Silla, within the ESO Key-Programme 1-004-43K. We wish to Thank to Dr. C. Bonatto for fruitful discussions. We also thank the anonymous referee for a number of useful suggestions. M. Pastoriza and F. Ferrari acknowledge CNPq and PRONEX/FINEP 76.97.1003.00 for financial support.

References

Binette L., Magris C.G., Stasinška G., Bruzual A.G., 1994, A&A 292, 13
Bonatto C., Pastoriza M.G., 1997, ApJ 486

de Vaucouleurs G., de Vaucouleurs A., Corwin H.G. Jr., et al., 1991 Third Reference Catalogue of Bright Galaxies. Springer-Verlag, New York
Forbes D., 1991, MNRAS 249, 779
Goudfrooij P., Hansen L., Jørgensen H.E., et al., 1994, A&AS 104, 179
Goudfrooij P., Hansen L., Jørgensen H.E., Nørgaard-Nielsen H.U., 1994, A&AS 105, 341
Goudfrooij P., Jong J. de, Hansen L., Nørgaard-Nielsen H.U., 1994, MNRAS 271, 833
Goudfrooij P., Jong T. de, 1995, A&A 278, 784
Kraan-Korteweg R.C., 1986, A&AS 66, 255
Macchetto F., Pastoriza M., Caon N., et al., 1996, A&A 120, 463 (Paper I)
Mathis J.S., Rumpl W., Nordsieck K.H., 1977, ApJ 217, 425
Poulain P., 1986, A&AS 64, 225
Poulain P., 1988, A&AS 72, 215
Poulain P., Nieto J.-L., 1994, A&AS 103, 573
Osterbrock D.E., 1974, Astrophysics of Gaseous Nebulae. Freeman W.H. & Co., San Francisco
Sandage A.R., Tammann G., 1987, A Revised Shapley-Ames Catalog of Bright Galaxies (2nd ed.). Carnegie, Washington
Spitzer L., 1978, Physical Processes in the Interstellar Medium. New York, Wiley
Van Dokkun P.G., Franx M., 1995, ApJ 110, 2027

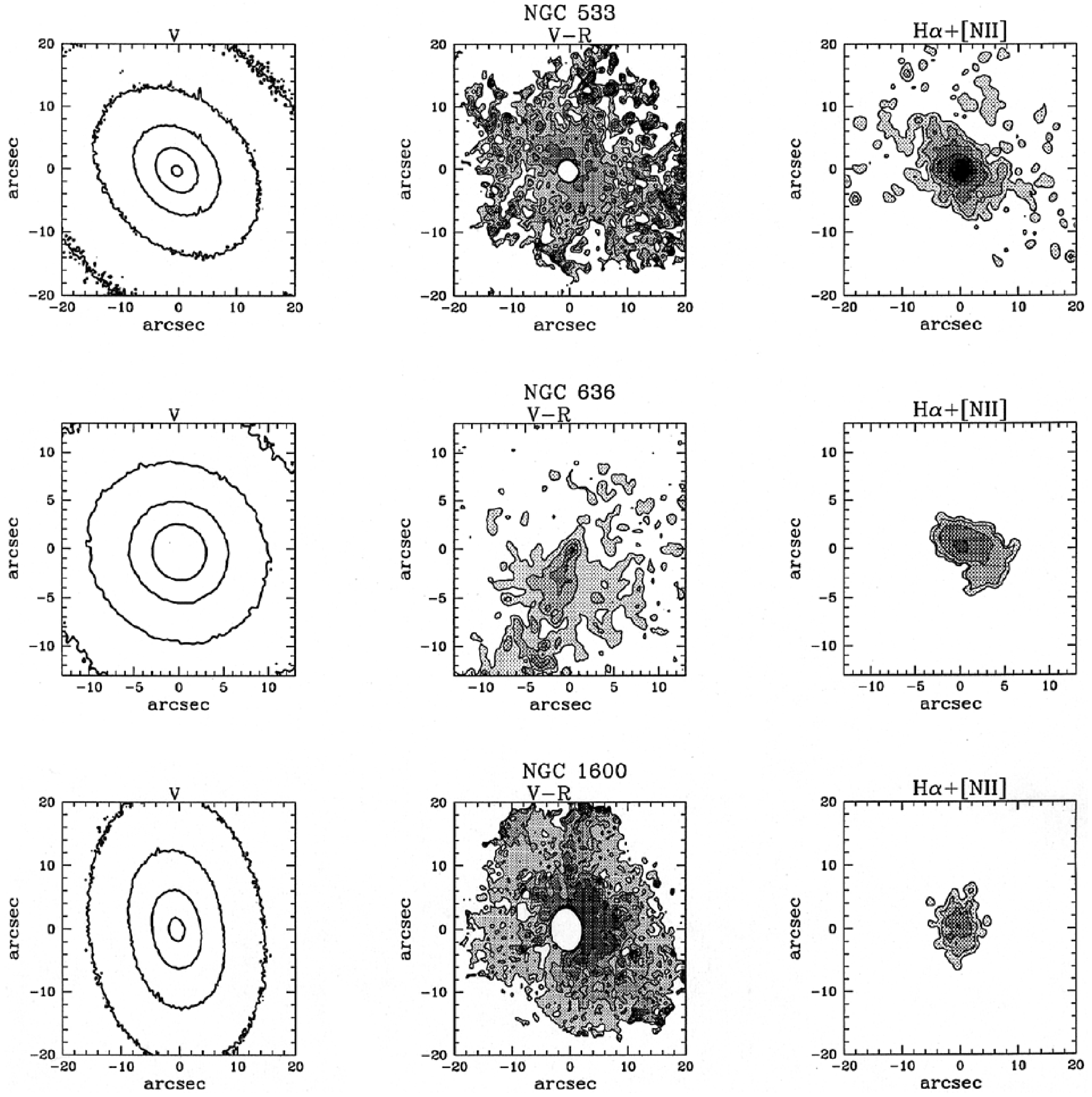

Fig. 5. NGC 533. V: 18, 19, 20, 21, 22; $(V-R)$: 0.55, 0.56, 0.57, 0.58; Hα + [NII]: 0.2; **NGC 636.** V: 18, 19, 20, 21; $(V-R)$: 0.56, 0.59, 0.62, 0.64; Hα + [NII]: 0.7; **NGC 1600.** V: 18, 19, 20, 21; $(V-R)$: 0.625, 0.63, 0.635, 0.64; Hα + [NII]: 0.5

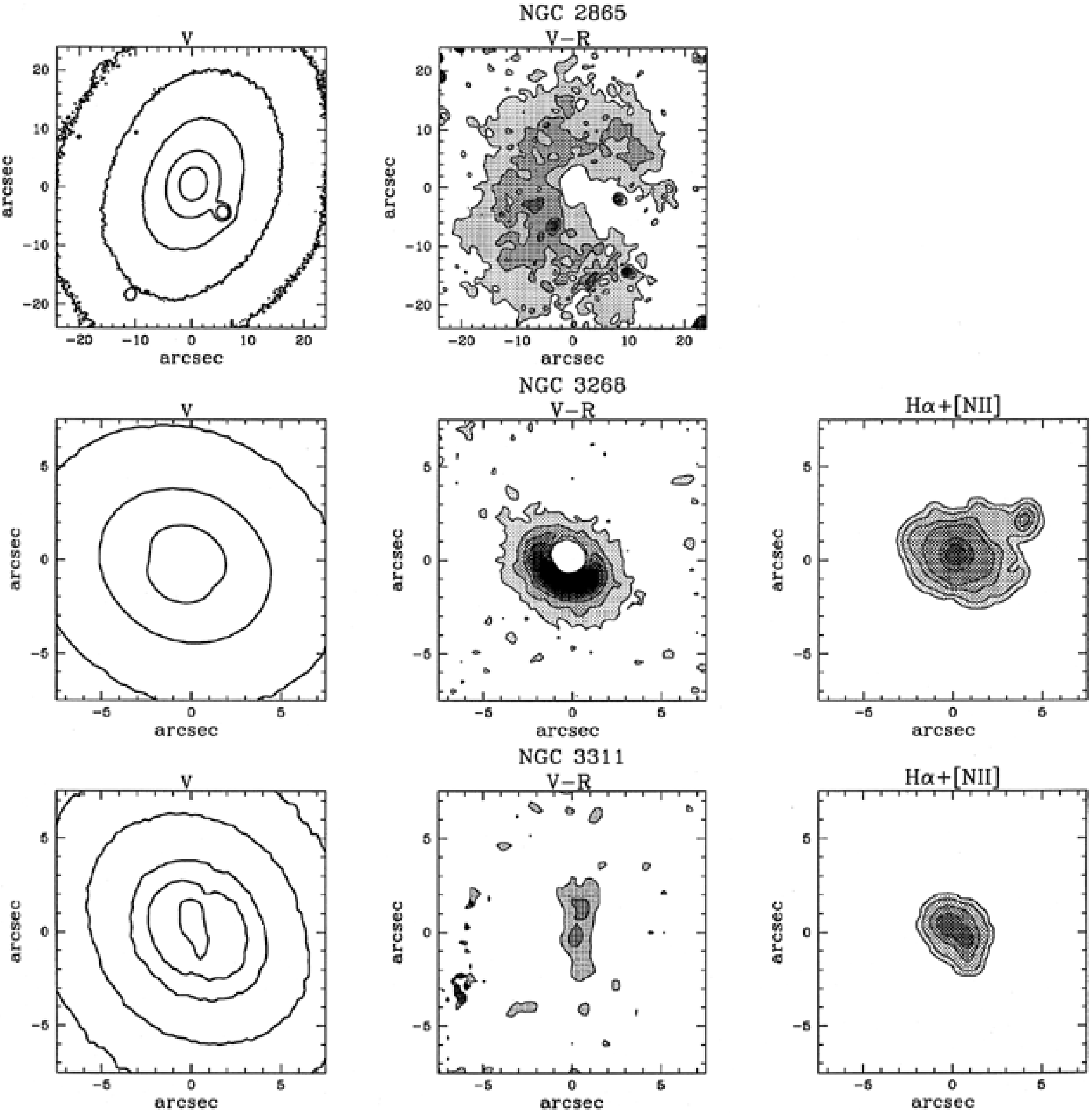

Fig. 5. NGC 2865. V: 18, 19, 20, 21, 22; $(V-R)$: 0.61, 0.62, 0.63, 0.64; **NGC 3268.** V: 18, 19, 20; $(V-R)$: 0.68, 0.7, 0.72, 0.74, 0.76, 0.78; Hα + [NII: 0.1; **NGC 3311.** V: 19.3, 19.5, 20, 20.5; $(V-R)$: 0.67, 0.69, 0.71; Hα + [NII]: 0.6

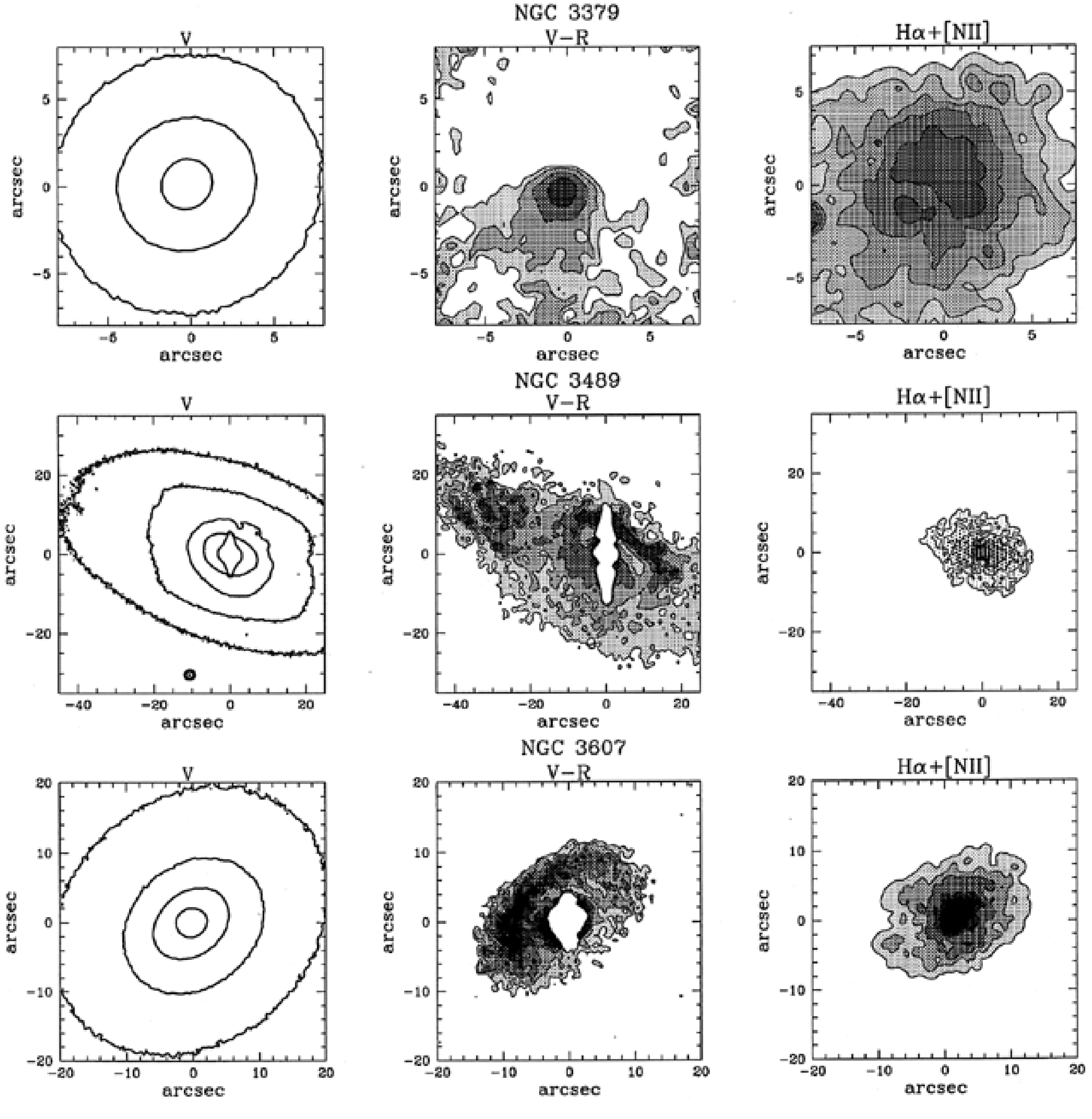

Fig. 5. NGC 3379. V: 16, 17, 18; $(V-R)$: 0.6, 0.61, 0.63, 0.66; Hα + [NII]: 0.6; **NGC 3489.** V: 17, 18, 19, 20, 21; $(V-R)$: 0.48, 0.50, 0.52, 0.54; Hα + [NII]: 1.7; **NGC 3607.** V: 17, 18, 19, 20; $(V-R)$: 0.59, 0.6, 0.61, 0.62, 0.63, 0.64; Hα + [NII]: 0.3

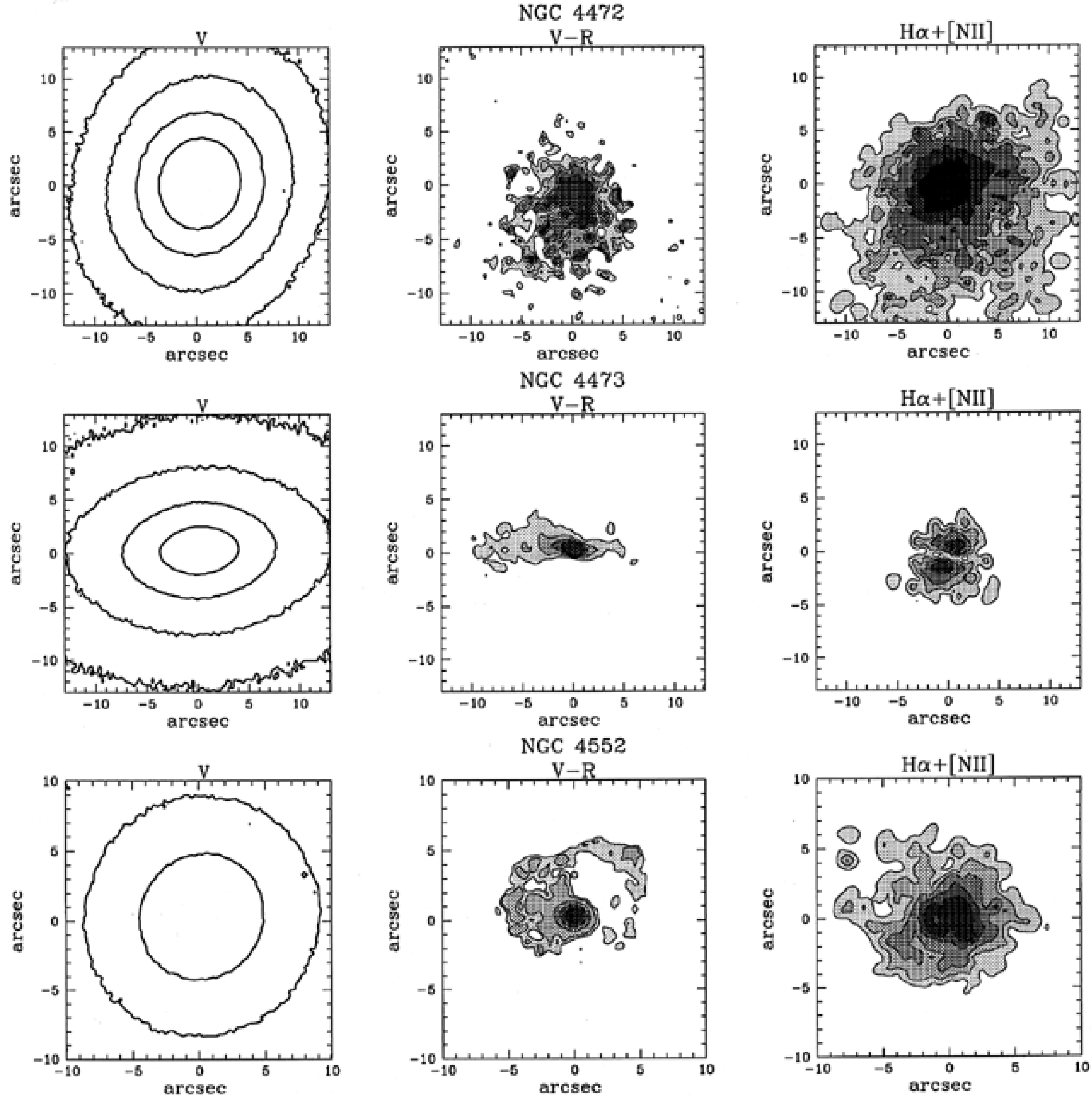

Fig. 5. NGC 4472. V: 17, 17.5, 18, 18.5; $(V-R)$: 0.605, 0.61, 0.615, 0.62; Hα + [NII]: 1.5; **NGC 4473.** V 17, 18, 19, 20; $(V-R)$: 0.68, 0.7, 0.72, 0.74; Hα + [NII]: 1.5; **NGC 4552.** V 16, 17, 18; $(V-R)$: 0.59, 0.595, 0.61, 0.63, 0.6; Hα + [NII]: 1.5

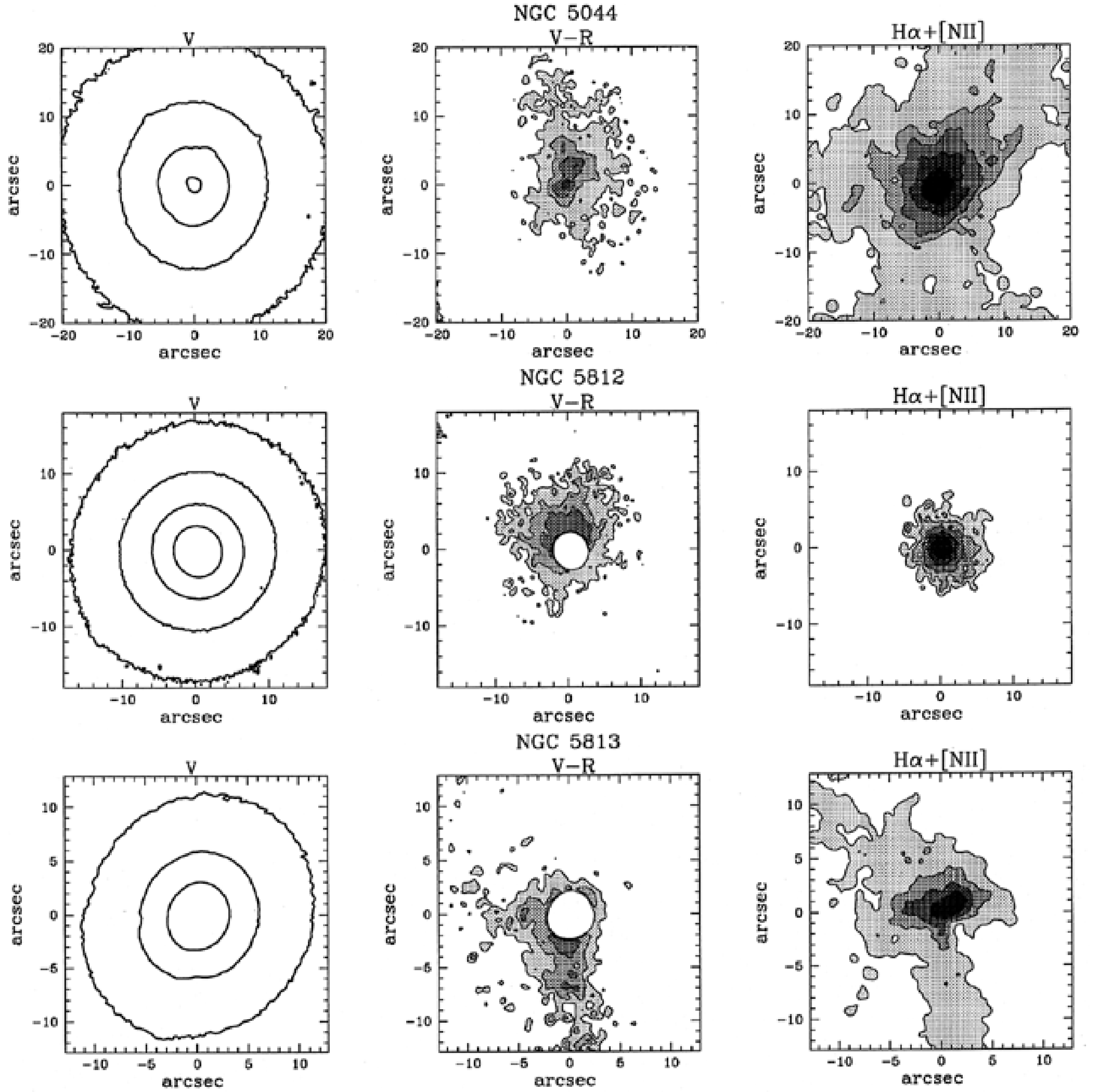

Fig. 5. NGC 5044. V: 18, 19, 20, 21; $(V-R)$: 0.66, 0.68, 0.7, 0.72; Hα + [NII]: 0.1; **NGC 5812.** V: 18, 19, 20, 21; $(V-R)$: 0.68, 0.69, 0.7; Hα + [NII]: 1.2; **NGC 5813.** V: 18, 19, 20; $(V-R)$: 0.67, 0.68, 0.69; Hα + [NII]: 1.2

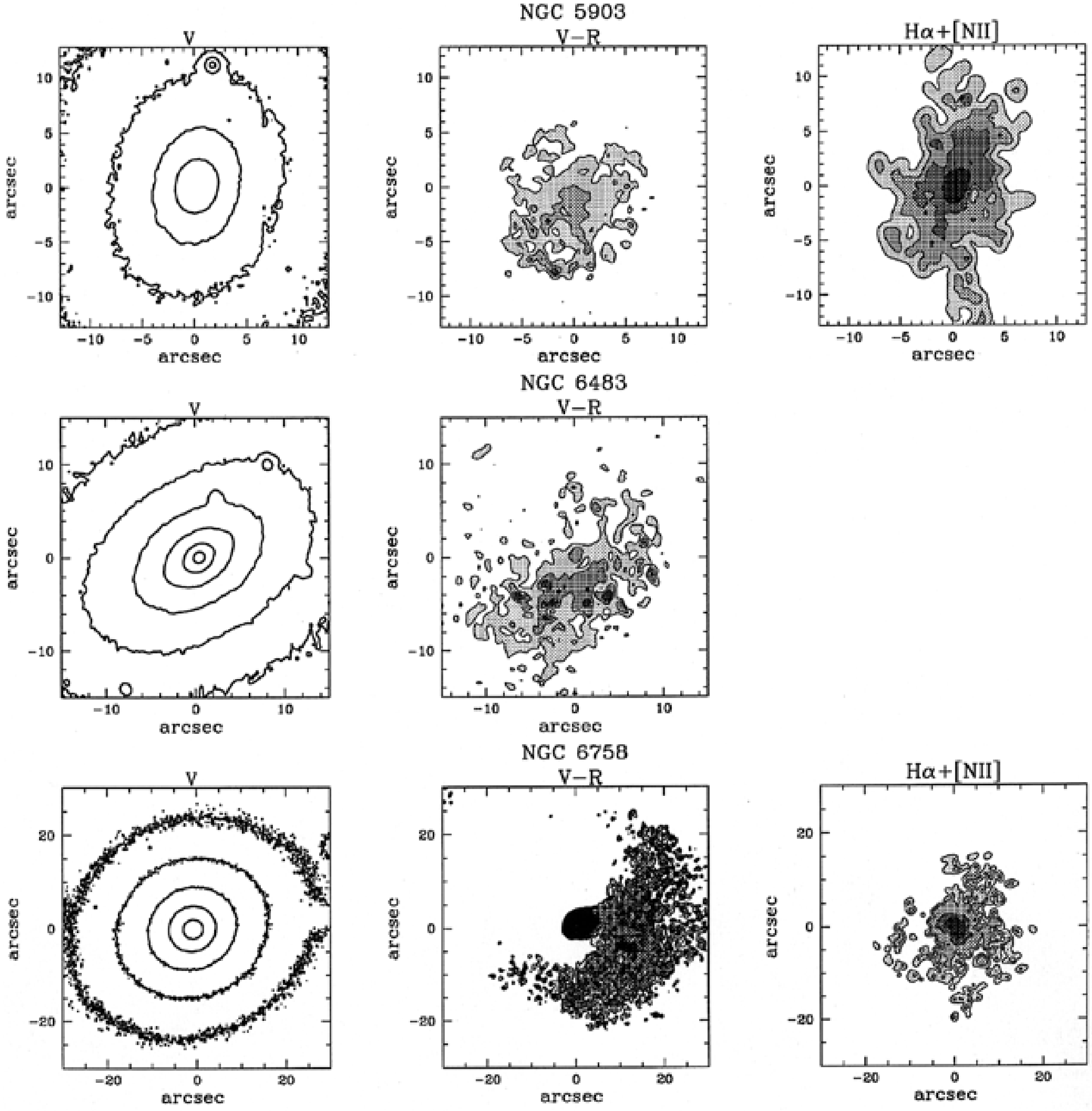

Fig. 5. NGC 5903. V: 18, 19, 20, 21; $(V-R)$: 0.65, 0.68, 0.7; $\mathrm{H}\alpha+$[NII]: 0.5; **NGC 6483.** V: 17, 18, 19, 20, 21, 22; $(V-R)$: 0.6, 0.62, 0.64; **NGC 6758.** V: 18, 19, 20, 21, 22; $(V-R)$: 0.6, 0.61, 0.62, 0.64, 0.66; $\mathrm{H}\alpha+$[NII]: 0.2

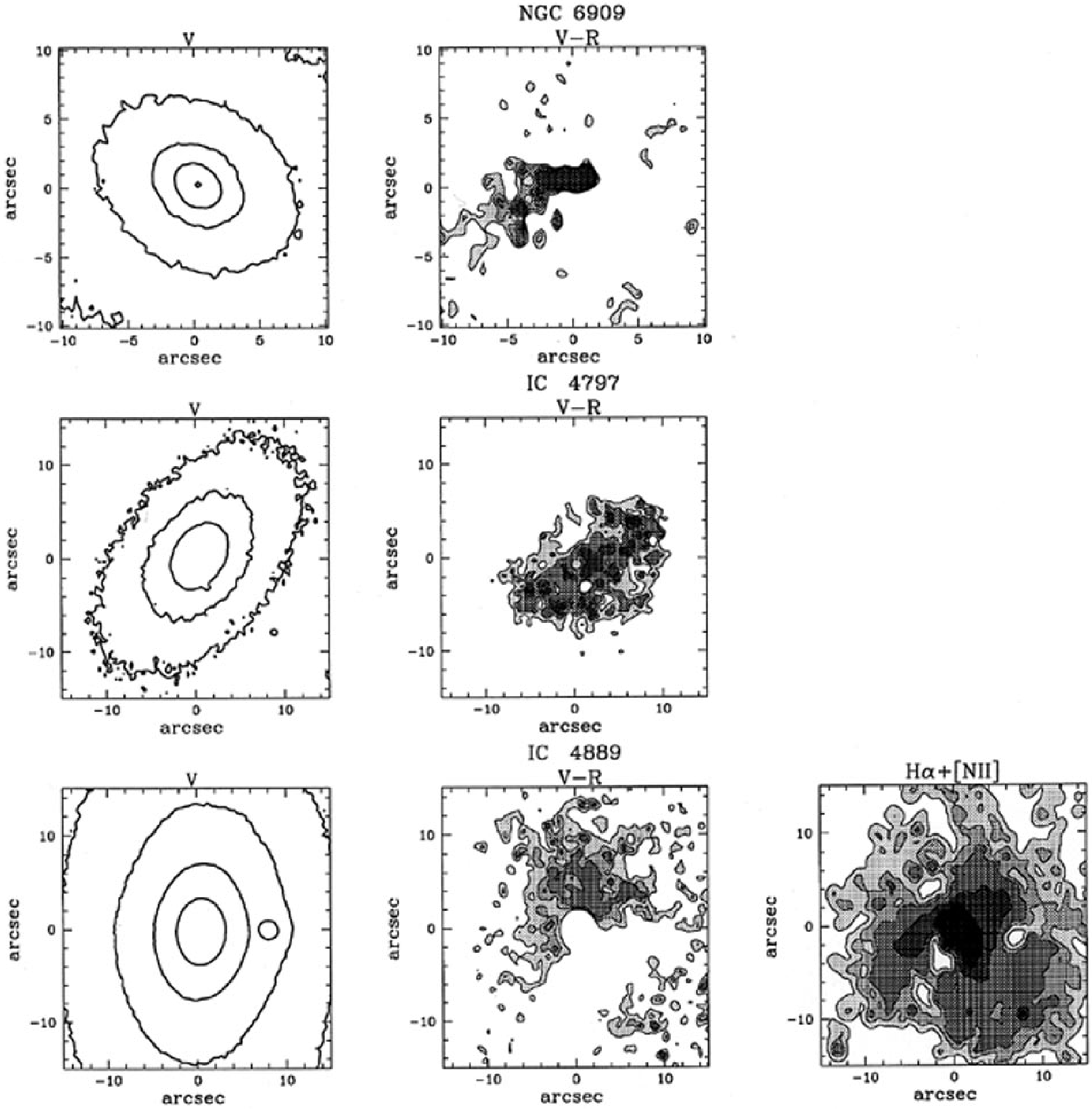

Fig. 5. NGC 6909. V: 17, 18, 19, 20, 21; $(V-R)$: 0.51, 0.52, 0.53, 0.54; **IC 4797.** V: 18, 19, 20; $(V-R)$: 0.58, 0.6, 0.63, 0.66; **IC 4889.** V: 18, 19, 20, 21; $(V-R)$: 0.616, 0.625, 0.63; $\mathrm{H}\alpha+$[NII]: 0.15

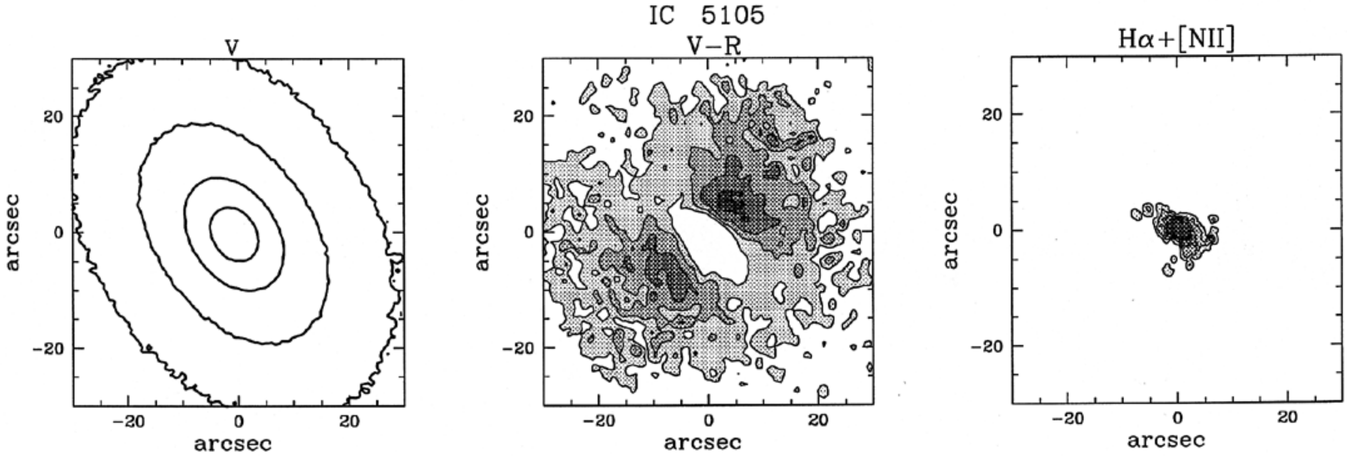

Fig. 5. IC 5105. V 18, 19, 20, 21; $(V-R)$: 0.61, 0.63, 0.65, 0.67; Hα + [NII]: 0.4